




RESEARCH ARTICLE | SEPTEMBER 25 2024

Early-time resonances in the three-dimensional wall-bounded axisymmetric Euler and related equations

Sai Swetha Venkata Kolluru   ; Rahul Pandit 



Physics of Fluids 36, 097159 (2024)

<https://doi.org/10.1063/5.0222257>



Articles You May Be Interested In

Real Schur flow computations, helicity fastening effects and Bagua-pattern cyclones

Physics of Fluids (October 2021)

Direct numerical simulations of the Taylor–Green vortex interacting with a hydrogen diffusion flame: Reynolds number and non-unity-Lewis number effects

Physics of Fluids (April 2023)



Physics of Fluids

Special Topics Open
for Submissions

[Learn More](#)

Early-time resonances in the three-dimensional wall-bounded axisymmetric Euler and related equations

Cite as: Phys. Fluids **36**, 097159 (2024); doi: 10.1063/5.0222257

Submitted: 6 June 2024 · Accepted: 31 August 2024 ·

Published Online: 25 September 2024



View Online



Export Citation



CrossMark

Sai Swetha Venkata Kolluru^{a)} and Rahul Pandit

AFFILIATIONS

Department of Physics, Indian Institute of Science, Bengaluru 560012, India

^{a)} Author to whom correspondence should be addressed: saik@iisc.ac.in

ABSTRACT

We investigate the complex-time analytic structure of solutions of the three-dimensional (3D)-axisymmetric, wall-bounded, incompressible Euler equations, by starting with the initial data proposed in Luo and Hou [“Potentially singular solutions of the 3D axisymmetric Euler equations,” Proc. Natl. Acad. Sci. U. S. A. **111**(36), 12968–12973 (2014)], to study a possible finite-time singularity. We use our pseudospectral Fourier–Chebyshev method [Kolluru *et al.*, “Insights from a pseudospectral study of a potentially singular solution of the three-dimensional axisymmetric incompressible Euler equation,” Phys. Rev. E **105**(6), 065107 (2022)], with quadruple-precision arithmetic, to compute the time-Taylor-series coefficients of the flow fields, up to a high order. We show that the resulting approximations display *early-time resonances*; the initial spatial location of these structures is different from that for the *tygers*, which we have obtained in Kolluru *et al.* [“Insights from a pseudospectral study of a potentially singular solution of the three-dimensional axisymmetric incompressible Euler equation,” Phys. Rev. E **105**(6), 065107 (2022)]. We then perform asymptotic analysis of the Taylor-series coefficients, by using generalized ratio methods, to extract the location and nature of the convergence-limiting singularities and demonstrate that these singularities are distributed around the origin, in the complex- t^2 plane, along two curves that resemble the shape of an eye. We obtain similar results for the one-dimensional (1D) wall-approximation (of the full 3D-axisymmetric Euler equation) called the 1D Hou–Luo model, for which we use Fourier-pseudospectral methods to compute the time-Taylor-series coefficients of the flow fields. Our work examines the link between tygers, in Galerkin-truncated pseudospectral studies, and early-time resonances, in truncated time-Taylor expansions of solutions of partial differential equations, such as those we consider.

Published under an exclusive license by AIP Publishing. <https://doi.org/10.1063/5.0222257>

I. INTRODUCTION

The regularity problem for hydrodynamical partial differential equations (PDEs), such as the three-dimensional (3D) Euler and the 3D Navier–Stokes equations^{3–5} has been the subject of several theoretical and numerical investigations over the last few decades. However, it is still not known whether the solutions of these PDEs, starting from smooth initial data, retain smoothness, for all time, or whether they lose regularity, at a finite time, leading to a *finite-time singularity* (often called *blowup* in common parlance).⁶ The breakdown of the regularity of solutions of the 3D Euler equations has been conjectured to play a key role in understanding of the structure of Navier–Stokes turbulence (see, e.g., Refs. 7–11).

The singularity problem for hydrodynamical PDEs has often been investigated by examining the analytic structure of solutions in the *complex-time domain*. The solution of the governing PDE is

represented as a Taylor series in integer powers n of the time t . The asymptotic behavior of these Taylor coefficients is determined by the dominant complex-time singularities that lie closest to the point about which the Taylor expansion is made. Early investigations of the finite-time-singularity problem for the 3D Euler equation, starting from Taylor–Green initial data,¹² used methods of asymptotic analysis that were developed originally for the study of singularities in critical phenomena,¹³ e.g., the ratio test¹⁴ and Padé-approximant methods.¹⁵ These methods were used in conjunction with high-precision arithmetic to study the analytic structure of Euler flows,^{12,16–18} high-Reynolds-number turbulent flows,¹⁹ and related hydrodynamical problems.^{20–22}

Over the years, direct-numerical-simulation (DNS) searches for possible singular solutions of hydrodynamical PDEs have grown apace with advances in high-performance computing, and state-of-the-art

numerical schemes have been developed to capture the growth of singular solutions. Complex-space singularities in solutions of such PDEs can be tracked by studying the temporal evolution of spectra by using the *analyticity-strip technique*.²³ However, as the solution proceeds toward finite-time blowup, the approximations of singular solutions, obtained by using finite-resolution and finite-precision numerical methods, often suffer from loss of accuracy or stability or both. This is because the flow fields develop increasingly small-scale structures for times close to the time of blowup.⁶

The fields are approximated by employing spectral methods in space; and the governing PDEs are solved via finite-difference time-marching schemes.^{24,25} The resulting numerical approximation is the exact solution of the spectrally truncated version of the governing PDE; but it deviates from the true solution of the PDE as the solution approaches the time of singularity (or potential singularity). These deviations first appear as localized, oscillatory structures in real space; they have been called *tygers*. Tygers were first reported in Fourier-pseudospectral approximations of the one-dimensional (1D) inviscid Burgers equation,²⁶ where they were attributed to nonlinear wave-particle resonances in regions of flow with positive strain. The spontaneous emergence of tygers in real space is accompanied by complex-space singularities crossing into the analyticity-strip of width Δ_x , where Δ_x is the smallest grid spacing in the domain. Tygers have also been reported in spectral studies of solutions of the 3D-axisymmetric, wall-bounded, incompressible Euler PDE² and of the 3D incompressible Euler PDE.²⁷

Recently, the complex-time analytic structure of solutions of the 1D inviscid Burgers equation has been re-investigated by using high-order time-Taylor-series methods.²⁸ Unlike earlier work, which concentrates on the singularity on the real time axis, Ref. 28 charts the landscape of singularities in the complex-time plane, by investigating the convergence of time-Taylor series of the 1D Burgers velocity field at each spatial point. For single- and multi-mode sine-wave initial data, the authors of Ref. 28 find several singularities, which are arranged in the form of an eye that is centered at the origin. Furthermore, they find that the truncated time-Taylor-series approximation of the velocity field shows spatially localized oscillatory structures, called *early-time resonances*, that are reminiscent of the tygers²⁶ mentioned above. These early-time resonances emerge at the spatial points at which the convergence of the Taylor-series expansion is first lost; and the corresponding complex-time singularities, situated off of the real time axis, are the convergence-limiting singularities.²⁸

We investigate the complex-time analytic structure of solutions of the 3D-axisymmetric, wall-bounded, incompressible Euler equations, starting from the initial data proposed in Ref. 1, to study a possible finite-time singularity. We use our pseudospectral Fourier-Chebyshev method,² with quadruple-precision arithmetic to compute the time-Taylor-series coefficients of the flow fields, up until a high order. The resulting approximations display early-time resonances; the initial spatial location of these structures is different from that for the tygers, which we have obtained in Ref. 2. We then perform asymptotic analysis of the Taylor-series coefficients, by using the Darboux-type ratio method due to Mercer and Roberts,²⁹ to extract the location and nature of the convergence-limiting singularities. We find that these singularities are distributed around the origin, in the complex- t^2 plane, along two curves that resemble the shape of an eye. We obtain similar results for the 1D wall-approximation, of the full 3D-axisymmetric

Euler equation, called the 1D Hou-Luo (HL) model.^{1,30} We use a Fourier-pseudospectral method,² with quadruple-precision arithmetic, to compute the time-Taylor-series coefficients of the flow fields. Our work examines early-time resonances, in truncated time-Taylor expansions of solutions of these PDEs, and compares them with tygers, in Galerkin-truncated pseudospectral studies.^{2,26}

The remaining part of this paper is organized as follows. For simplicity, we first discuss the 1D HL model and obtain and analyze time-Taylor series for its solutions in Sec. II A. We then discuss and analyze the time-Taylor series for solutions of the 3D-axisymmetric wall-bounded incompressible Euler equations in Sec. II B. We present our results for the 1D HL model in Sec. III A, including the complex-singularity landscape. We present similar results for the 3D-axisymmetric wall-bounded incompressible Euler equations in Sec. III B. Finally, in Sec. IV, we conclude with a discussion of our results. In Appendixes A and B, we give, respectively, a Mathematica code for the symbolic computation of time-Taylor coefficients for the 1D HL model and some details of the Mercer-Roberts method.

II. MODELS AND METHODS

A 1D wall-approximation for the full 3D-axisymmetric incompressible Euler (3DAE) equation was developed by Luo and Hou.¹ It is now called the 1D HL model.³⁰ We discuss this 1D HL model first, in Sec. II A 1, because it is much simpler than the full 3DAE (see below). We construct the time-Taylor-series representation for solutions of the 1D HL model and derive recursion relations for these time-Taylor coefficients in Sec. II A 2. We describe the Fourier-pseudospectral methods and the numerical computation of the coefficients for this model in Sec. II A 3. In Sec. II B 1, we describe the 3DAE; and we derive the recursion relations for the time-Taylor coefficients of the series for the fields in Sec. II B 2. Fourier-Chebyshev pseudospectral methods, which we use for the computation of these coefficients, are presented in Sec. II B 3.

A. 1D HL model

1. Model

The 1D HL model approximates the singular dynamics of the 3DAE [see Eq. (7) below], at the wall at $r = 1$, as discussed in Refs. 1, 2, and 30. This model is

$$\partial_t u + v \partial_z u = 0, \quad (1a)$$

$$\partial_t \omega + v \partial_z \omega = \partial_z u, \quad (1b)$$

$$\partial_z v = \mathcal{H}[\omega], \quad (1c)$$

where $\mathcal{H}[\cdot]$ is the Hilbert transform operator; u , ω , and v are related, respectively, to the angular components of the velocity, vorticity, and stream function in the 3DAE (see below) at $r = 1$; and Eq. (1c) is the Biot-Savart-type law for this model. The domain is periodic in z with the periodicity length $L = 2\pi$.

2. Time-Taylor-series expansion and recursion relations

We write the time-Taylor expansions

$$u(z, t) = \sum_{n=0}^{\infty} u_n(z) t^n, \quad (2a)$$

$$\omega(z, t) = \sum_{n=0}^{\infty} \omega_n(z) t^n, \tag{2b}$$

$$v(z, t) = \sum_{n=0}^{\infty} v_n(z) t^n, \tag{2c}$$

where $u_n(z)$, $\omega_n(z)$, and $v_n(z)$ are time-Taylor coefficient of order n , which are functions of z . Hereafter, we suppress the dependence on z for notational simplicity. To construct recursion relations for the time-Taylor coefficients, we substitute the series expansions (2a)–(2c) in Eqs. (1a)–(1c). By comparing coefficients of terms of degree t^{n+1} , we obtain

$$u_n = \frac{-1}{n} \sum_{l+m=n-1} v_l \partial_z u_m, \quad n > 0, \tag{3a}$$

$$\omega_n = \frac{-1}{n} \sum_{l+m=n-1} v_l \partial_z \omega_m + \frac{1}{n} \partial_z u_{n-1}, \quad n > 0, \tag{3b}$$

and

$$v_n = \int \mathcal{H}(\omega_n(z')) dz', \quad n > 0. \tag{3c}$$

The initial conditions are $u_0(z) = u(z, t = 0)$, $\omega_0(z) = \omega(z, t = 0)$, and $v_0(z) = \int \mathcal{H}(\omega_0(z')) dz'$.

Once the initial data are specified, we can use the recursion relations in Eq. (3) to derive closed-form expressions for $u_n(z)$, $\omega_n(z)$, and $v_n(z)$, analytically. However, the derivation of high-order coefficients quickly becomes cumbersome, even if we use symbolic-computation software (see Appendix A for details). Therefore, we compute the time-Taylor coefficients on a finite grid by using quadruple-precision Fourier-pseudospectral numerical methods.

3. Fourier-pseudospectral methods

In the L -periodic domain, we define a uniform collocation grid of N points given by $\mathbf{X}_N = \{z_j = j\Delta z : j = 0, 1, \dots, N - 1\}$, where $\Delta z = L/N$. The Fourier-pseudospectral projection operation P_N is

$$P_N u(z, t) = \sum_{|k| \leq N/2} \hat{u}(k, t) e^{\frac{i2\pi k z}{L}}; \tag{4a}$$

$$\hat{u}(k, t) = \frac{1}{N} \sum_{j=0}^{N-1} u(z_j, t) e^{-\frac{i2\pi k z_j}{L}}. \tag{4b}$$

Given the initial data $u_0(z)$, $\omega_0(z)$, and $v_0(z)$, we first perform a pseudospectral projection to obtain $P_N u_0$, $P_N \omega_0$, and $P_N v_0$ by using the FFTW3 library.³¹ To compute $u_n(\mathbf{X}_N) := \{u_n(z) : z \in \mathbf{X}_N\}$, we set $n = 1$ in Eq. (3a). We evaluate the derivative $\partial_z u_n$ on the right-hand side (RHS) of Eq. (3a) in Fourier spectral space. The nonlinear terms are computed in real space. Similarly, we evaluate $\omega_1(\mathbf{X}_N)$ from Eq. (3b). We use $\omega_1(\mathbf{X}_N)$ to compute $v_1(\mathbf{X}_N)$ from Eq. (3c); the integration is performed in Fourier spectral space. The values of $u_1(\mathbf{X}_N)$, $\omega_1(\mathbf{X}_N)$, and $v_1(\mathbf{X}_N)$ can then be used to compute the values of $u_2(\mathbf{X}_N)$, $\omega_2(\mathbf{X}_N)$, and $v_2(\mathbf{X}_N)$. We repeat this procedure for $n \geq 2$.

B. 3D-axisymmetric wall-bounded incompressible Euler equation

1. Model

We now consider the 3D Euler equation in the vorticity–stream function formulation,

$$\omega_t + \mathbf{u} \cdot \nabla \omega = \omega \cdot \nabla \mathbf{u}, \tag{5}$$

where $\omega = \nabla \times \mathbf{u}$ is the vorticity, $\mathbf{u} = \nabla \times \psi$ is the velocity field, and ψ is the vector-valued stream function. The Poisson equation $\omega = -\nabla^2 \psi$ gives the relation between the vorticity and the stream function.

To represent axisymmetric fields, we use $\mathbf{u}(r, z) = u^r(r, z) \hat{\mathbf{e}}_r + u^\theta(r, z) \hat{\mathbf{e}}_\theta + u^z(r, z) \hat{\mathbf{e}}_z$, where $\hat{\mathbf{e}}_r$, $\hat{\mathbf{e}}_\theta$, and $\hat{\mathbf{e}}_z$ are unit vectors in the cylindrical coordinate system. Furthermore, we define new variables in terms of the angular components u^θ , ω^θ , and ψ^θ ,

$$u^1 = u^\theta / r; \quad \omega^1 = \omega^\theta / r; \quad \psi^1 = \psi^\theta / r. \tag{6}$$

The 3D-axisymmetric wall-bounded incompressible Euler (3DAE) equations are then given in terms of the new variables (6) by

$$u_t^1 + u^r u_r^1 + u^z u_z^1 = 2u^1 \psi_z^1, \tag{7a}$$

$$\omega_t^1 + u^r \omega_r^1 + u^z \omega_z^1 = ((u^1)^2)_z, \tag{7b}$$

$$-\left(\partial_r^2 + \frac{3}{r} \partial_r + \partial_z^2\right) \psi^1 = \omega^1, \tag{7c}$$

with $u^r = -r\psi_z^1$ and $u^z = 2\psi^1 + r\psi_r^1$. For a detailed derivation, see pp. 64–66 of Ref. 32 and Refs. 1 and 33. So long as the solutions to Eq. (7) are smooth [$C^\infty(\mathbf{R} \times \bar{\mathbf{R}}^+)$], u^θ , ω^θ , and ψ^θ all vanish at $r = 0$; this ensures that the coordinate singularity at $r = 0$ does not enter the evolution equations (7) directly.³⁴ Here, \mathbf{R} represents the set of real numbers, and $\bar{\mathbf{R}}^+$ represents the set of affinely extended positive real numbers.

We solve Eq. (7) in the domain $D(1, L) = \{(r, z) : 0 \leq r \leq 1, 0 \leq z \leq L\}$, with L -periodic boundary conditions along $\hat{\mathbf{e}}_z$, the no-flow conditions at $r = 1$ (8a), and the following pole conditions at $r = 0$ (8b):

$$\psi^1(r = 1, z, t) = 0; \tag{8a}$$

$$u_r^1(r = 0, z, t) = \omega_r^1(r = 0, z, t) = \psi_r^1(r = 0, z, t) = 0. \tag{8b}$$

The 3D-axisymmetric field variables in Eq. (7) at $r = 1$ can be approximated by the 1D-HL-model (1) fields in Eq. (1) as discussed in Ref. 1,

$$\begin{aligned} u(z) &\rightarrow (u^1)^2(r = 1, z), & \omega(z) &\rightarrow \omega^1(r = 1, z), \\ v(z) &\rightarrow \partial_r \psi^1(r = 1, z). \end{aligned} \tag{9}$$

2. Time-Taylor-series expansion and recursion relations

We write the time-Taylor-series expansions for the fields $u^1(r, z, t)$, $\omega^1(r, z, t)$, and $\psi^1(r, z, t)$ as

$$u^1(r, z, t) = \sum_{n=0}^{\infty} u_n^1(r, z) t^n, \quad \omega^1(r, z, t) = \sum_{n=0}^{\infty} \omega_n^1(r, z) t^n,$$

and

$$\psi^1(r, z, t) = \sum_{n=0}^{\infty} \psi_n^1(r, z) t^n. \tag{10}$$

Similarly, we write $u^r(r, z, t) = \sum_{n=0}^{\infty} u_n^r(r, z) t^n$ and $u^z(r, z, t) = \sum_{n=0}^{\infty} u_n^z(r, z) t^n$ for the radial and axial velocities, respectively. By substituting these series expansions for the fields in Eqs. (7a)–(7c) and equating the coefficients of t^{n+1} on both sides, we obtain

$$u_n^1(r, z) = -\frac{1}{n} \sum_{l+m=n-1} (u_l^r \partial_r u_m^1 + u_l^z \partial_z u_m^1 - 2u_l^1 \partial_z \psi_m^1); \quad (11a)$$

$$\omega_n^1(r, z) = -\frac{1}{n} \sum_{l+m=n-1} (u_l^r \partial_r \omega_m^1 + u_l^z \partial_z \omega_m^1 - \partial_z (u_l^1 \omega_m^1)). \quad (11b)$$

Once we determine $\omega_n^1(r, z)$, we use the Poisson equation (7c) to obtain $\psi_n^1(r, z)$ as follows:

$$-\left(\partial_r^2 + \frac{3}{r} \partial_r + \partial_z^2\right) \psi_n^1 = \omega_n^1; \quad (11c)$$

$$\partial_r \psi_n^1(r = 0, z) = 0; \quad \psi_n^1(r = 1, z) = 0. \quad (11d)$$

Here, the boundary conditions in Eqs. (8a) and (8b) are applied to $\psi_n^1(r, z)$ in Eq. (11d). We can then obtain the time-Taylor coefficients for the radial and axial velocity fields,

$$u_n^r = (-r \partial_z) \psi_n^1; \quad (11e)$$

$$u_n^z = (2 + r \partial_r) \psi_n^1. \quad (11f)$$

The initial data are used to define u_0^1 , ω_0^1 , and ψ_0^1 (cf. Subsection II A 2 for the 1D HL model). For $n = 1$, $u_1^1(r, z)$ and $\omega_1^1(r, z)$ can be obtained analytically, as closed-form expressions, by using Eqs. (11a) and (11b). However, unlike the Biot-Savart law for the 1D HL model in Eq. (1c), the Poisson equation in Eqs. (11c) and (11d) cannot be solved analytically for $\psi_1^1(r, z)$ via symbolic computation. Thus, we use our Fourier-Chebyshev pseudospectral scheme² with quadruple-precision arithmetic. We describe our methods briefly in Subsection II B 3 (for details see Ref. 2).

3. Fourier-Chebyshev pseudospectral method for the computation of time-Taylor coefficients

We discretize the domain by using the collocation grid $\mathbf{X}_{N,M} := \{(r_i, z_j) : i = 1, \dots, N \text{ and } j = 0, \dots, M - 1\}$, where the axial nodes $\{z_j = \frac{Lj}{M}\}_{j=0, \dots, M-1}$ are uniformly spaced. The radial nodes $\{r_i = \frac{1}{2}(1 + \cos(\frac{\pi(i-0.5)}{N}))\}_{i=1, \dots, N}$, the roots of the highest-order Chebyshev polynomial $T_N(2r - 1)$ in the spectral basis, are non-uniformly spaced and cluster near $r = 0$ and $r = 1$. The Fourier-Chebyshev pseudospectral approximation for the field $u^1(r, z, t)$ is then given by

$$P_{N,M} u^1(r, z, t) = \sum_{|k| < M/2} \sum_{l=0}^N \hat{u}^1(k, l, t) e^{ikz} T_l(2r - 1), \quad (12)$$

where $T_l(x)$ is the order- l Chebyshev polynomial of the first kind.

We compute the derivative terms in spectral space. The Poisson problem in Eqs. (11c) and (11d) is solved by using the Fourier-Chebyshev Tau Poisson solver described in Refs. 2 and 35. The nonlinear terms are computed in real space. Given the initial data $u_0^1(\mathbf{X}_{N,M})$, $\omega_0^1(\mathbf{X}_{N,M})$, and $\psi_0^1(\mathbf{X}_{N,M})$, we compute $u_1^1(\mathbf{X}_{N,M})$ and $\omega_1^1(\mathbf{X}_{N,M})$ from Eqs. (11a) and (11b). We then solve the Poisson problem (11c) and (11d) for $\psi_1^1(\mathbf{X}_{N,M})$. We repeat this process to obtain the time-Taylor coefficients for $n = 2, 3, \dots, N_t$, where N_t is the order at which we truncate the time-Taylor expansion in Eq. (10). The choice of N_t plays a crucial role in ensuring that the results of our asymptotic analysis are accurate (see Sec. III B for details): time-Taylor coefficients, computed for $n > N_t$, suffer from errors that arise because

of (a) fixed-precision arithmetic and (b) the finite number of modes retained in any implementation of the pseudospectral method.

III. RESULTS

We compute and examine the time-Taylor coefficients for special choices of initial data that lead to (possible) finite-time singularities.² We then perform asymptotic analysis^{14,29,36} of these coefficients to estimate the position and the nature of the convergence-limiting singularities. In Sec. III A, we chart out the pattern of these singularities for a singular solution of the 1D HL model (1). In Sec. III B, we repeat the analysis for the potentially singular solution of the 3DAE equation (7) with the initial condition used in Refs. 1, 2, 37, and 38.

A. 1D HL model

We start with the following initial data:

$$u_0(z) = \sin^2(z); \quad \omega_0(z) = 0. \quad (13)$$

It has been proved³⁰ that the flow, which evolves from Eq. (13), develops a finite-time singularity. For a scaled version of the initial data used in Ref. 2, the time of singularity lies near $t_* \simeq 0.0035$.

We now apply the recursion relations in Eqs. (3a)–(3c), starting from the initial data in Eq. (13). We use symbolic computation to compute the closed-form expressions, for low-order ($n \leq 7$) coefficients $u_n(z)$, $\omega_n(z)$, and $v_n(z)$, that we list in Table I. Appendix A contains our Mathematica code for the determination of these coefficients. The odd-order coefficients for $u(z)$ and the even-order coefficients for $\omega(z)$ and $v(z)$ vanish identically because of the symmetry of the initial data (13). The difficulty of symbolic computation and the storage of high-order coefficients increases rapidly with the order n . Therefore, we use the Fourier-pseudospectral methods outlined in Sec. II A 3 to compute the time-Taylor coefficients up to order $n \leq N_t = 100$, on a uniform grid with $N = 256$ points. For accuracy, it is important to use quadruple-precision arithmetic. In Fig. 1, we present a sign-coded heat map of the absolute values of the coefficients $u_n(z)$, $\omega_n(z)$, and $\psi_n(z)$ for $n \leq 100$ evaluated at the collocation points $z \in \mathbf{X}_{N=256}$; the coefficients with positive (negative) signs are shown in red (blue); the color bars use a log scale (base 10). White regions appear in these plots where the coefficients vanish identically [e.g., for odd orders in $u_n(z)$] or fall below 10^{-15} .

In Fig. 2, we plot the truncated series approximations $u_{N_t} := \sum_{n=0}^{N_t} u_n t^n$, $\omega_{N_t} := \sum_{n=0}^{N_t} \omega_n t^n$, and $v_{N_t} := \sum_{n=0}^{N_t} v_n t^n$ at time $t = 1.13$, for $N_t = 10$ (yellow), 30 (blue), and 100 (red). We observe the emergence of localized oscillatory structures at $z = \{\frac{\pi}{4}, \frac{3\pi}{4}, \frac{5\pi}{4}, \frac{7\pi}{4}\}$, for all the fields; we refer to these structures as *early-time resonances*, a term introduced in Ref. 28 for the 1D inviscid Burgers equation in a periodic domain. Similar oscillatory structures were also reported for the Fourier-pseudospectral study of the 1D HL model in Ref. 2, near the time of singularity; they were identified as nonlinear wave-particle resonances called *tygers*. However, the spatial locations of the tygers, observed in Ref. 2 for $u(z, t)$ and $\omega(z, t)$, are different from what we see in Fig. 2: In particular, for the initial condition (13), the Fourier-pseudospectral study in Ref. 2 yields tygers at $z = \{\frac{\pi}{2}, \frac{3\pi}{2}\}$ for $u(z, t)$ and $\omega(z, t)$. This dissimilarity between early-time resonances and tygers, which we observe here, generalizes significantly its first observation in Ref. 28 for the 1D inviscid Burgers equation.

In Fig. 2, the emergence of early-time resonances signals the loss of convergence of the Taylor-series approximation. For an analytic

TABLE I. Closed-form symbolic expressions of the time-Taylor coefficients $u_n(z)$, $\omega_n(z)$, and $v_n(z)$ for low-order $n \leq 7$, obtained by using the recursion relations in Eq. (3) and starting from the initial data in Eq. (13) (see Appendix A for details).

n	$u_n(z)$	$\omega_n(z)$	$v_n(z)$
0	$\sin^2(z)$	0	0
1	0	$\sin(2z)$	$\sin(z)(-\cos(z))$
2	$\sin^2(z) \cos^2(z)$	0	0
3	0	$\frac{1}{3} \sin(4z)$	$-\frac{1}{12} \sin(4z)$
4	$\frac{1}{12} \sin(2z) \sin(4z)$	0	0
5	0	$\frac{1}{15} (2 \sin(6z) - \sin(2z))$	$\frac{1}{90} (3 \sin(2z) - 2 \sin(6z))$
6	$\frac{1}{270} \sin^2(2z)(17 \cos(4z) + 7)$	0	0
7	0	$\frac{109 \sin(8z) - 86 \sin(4z)}{1890}$	$\frac{172 \sin(4z) - 109 \sin(8z)}{15120}$
.	.	.	.
.	.	.	.

function $u(t)$, the convergence of the Taylor series about a point $t = t_0$ is limited by the nearest singularity in the complex- t plane. If R is the distance of the nearest singularity from the point of expansion t_0 , the Taylor series loses convergence for $|t - t_0| > R$. The nature and position of this singularity (or singularities) governs the large- n behavior of the Taylor coefficients. Conversely, we can use the large- n behavior of $u_n(z)$, $\omega_n(z)$, and $v_n(z)$ in Fig. 1 to chart the positions of complex-time singularities.

Given our initial data (13), the time-Taylor-series expansion for $u(z, t)$ (Table I) contains only even-order terms, so we use $q \equiv t^2$ as the expansion variable. In contrast, the expansions for $\omega(z, t)$ and $v(z, t)$ do not have even-order terms in t ; this allows us to rewrite their series in terms of $q \equiv t^2$, with a prefactor of $t = q^{1/2}$ as follows:

$$u_{N_i}(z, q) = \sum_{n=0}^{N_i/2} u_{2n}(z) q^n; \tag{14a}$$

$$\omega_{N_i}(z, q) = q^{1/2} \sum_{n=0}^{N_i/2} \omega_{2n+1}(z) q^n; \tag{14b}$$

$$v_{N_i}(z, q) = q^{1/2} \sum_{n=0}^{N_i/2} v_{2n+1}(z) q^n. \tag{14c}$$

Furthermore, in Fig. 1, we observe that $u_{2n}(z = 0)$ and $u_{2n}(z = \pi)$ display alternating signs with a long period; the period over which the sign of the coefficient alternates is reduced as $z \rightarrow \{\pi/2\}$. Given these alternating signs, we cannot use the standard Domb-Sykes ratio method^{14,36} for determining the radius of convergence of the series $u_{N_i}(z, t)$. This method can only be applied when the coefficients are all of the same sign or have strictly alternating signs. When the signs alternate with a period greater than 1, the sign of the ratio $u_{2(n+1)}(z)/u_{2n}(z)$ changes with n , so $u_{2(n+1)}(z)/u_{2n}(z)$ does not have a well-defined limit as $n \rightarrow \infty$.

Mercer and Roberts²⁹ (MR) generalized the Domb-Sykes method for series with coefficients whose signs change with order n and have a period of alternation greater than 1. In the MR method, the pattern of alternating signs is attributed to a pair of complex-conjugate singularities that lie close to the real domain (see Appendix B). For a given value of z , the Taylor series $u_{N_i}(z, q)$ is approximated by the

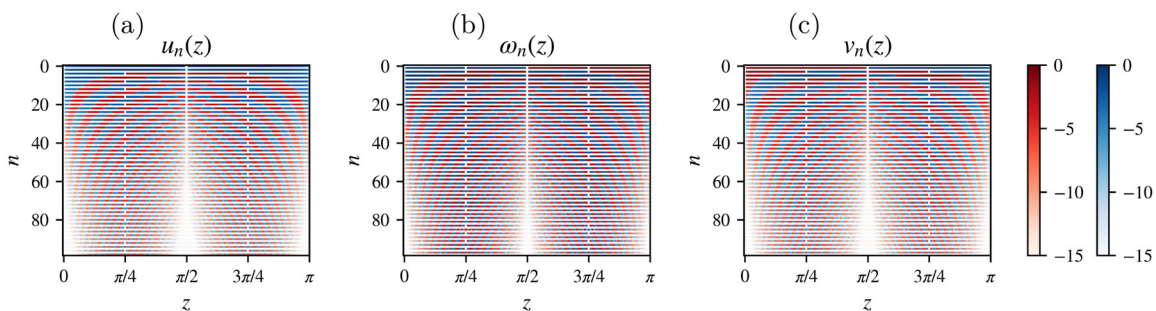


FIG. 1. Sign-coded heat maps of the absolute values of the time-Taylor coefficients (a) $u_n(z)$, (b) $\omega_n(z)$, and (c) $v_n(z)$, for $n \leq 100$ evaluated at $z \in \mathbf{X}_{N-256}$. The coefficients with positive (negative) signs are shown in red (blue); $u_n(z)$ vanishes identically for odd n (white bands); and $\omega_n(z)$ and $v_n(z)$ vanish identically for even n , because of the symmetry in the initial condition. We use a log scale (base 10) for the color bar.

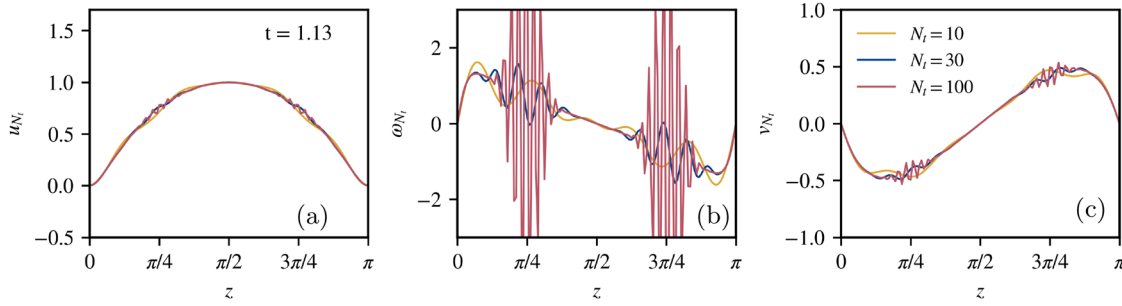


FIG. 2. Plots vs z of the truncated time-Taylor-series approximations for the fields (a) $u_{N_t}(z, t)$, (b) $\omega_{N_t}(z, t)$, and (c) $v_{N_t}(z, t)$ at time $t = 1.13$, summed for $N_t = 10$ (yellow), 30 (blue), and 100 (red). Early-time resonances, which occur in all three fields, are oscillatory structures localized around $z = \{\frac{\pi}{4}, \frac{3\pi}{4}\}$; their amplitude is largest for ω_{N_t} .

MR-model function $u(z, \mathbf{q})$, in complex- \mathbf{q} space, where \mathbf{q} is the complexified version of the variable $q = t^2$,

$$u(z, \mathbf{q}) = \left(1 - \frac{\mathbf{q}}{\mathbf{q}_*}\right)^{\nu(z)} + \left(1 - \frac{\mathbf{q}}{\bar{\mathbf{q}}_*}\right)^{\nu(z)}; \quad \mathbf{q}_*(z) := R(z)e^{i\theta(z)}. \tag{15}$$

Here, \mathbf{q}_* denotes the position of the convergence-limiting complex singularity and $\bar{\mathbf{q}}_*$ its complex-conjugate. The unknown functions $R(z) > 0$, $\theta(z) \in [0, \pi]$, with $\nu(z) \in \mathbb{R}$ neither zero nor a positive integer. For each value of $z \in \mathbf{X}_{N_t}$, we construct the MR coefficients $B_k^2(z)$ given in Eq. (16a). We then perform a nonlinear fit for B_k^2 with the functional forms given in Eq. (16b) below:

$$B_k^2(z) = \frac{u_{k+1}(z) \cdot u_{k-1}(z) - u_k^2(z)}{u_k(z) \cdot u_{k-2}(z) - u_{k-1}^2(z)}; \quad 2 \leq k \leq (N_t - 1); \tag{16a}$$

$$u_n(z) = 2(-1)^n \binom{\nu(z)}{n} R(z)^{-n} \cos(n\theta(z)); \quad 0 \leq n \leq N_t. \tag{16b}$$

From these, we obtain estimates for the functions $R(z)$, $\theta(z)$, and $\nu(z)$ [Figs. 3(a)–3(c), respectively], for $z \in \mathbf{X}_{256}$, by using the LMFIT package³⁹ in Python. In Appendix B, we discuss the $\frac{1}{k}$ linear fit for $B_k(z)$; this linear fit works for $z = \{0, \frac{\pi}{8}\}$; for other values of z , we must, perforce, use the nonlinear fit provided by LMFIT. The estimates from Eqs. (14a), (14b), and (14c) are shown, respectively, in yellow, pink, and blue in Figs. 3(a)–3(c).

The convergence-limiting singularities for $z = \{0, \pi\}$ occur at $\theta(0) = \theta(\pi) = 0$; and for $z = \frac{\pi}{2}$ they occur at $\theta(\frac{\pi}{2}) = \pi$ [panel (b) of Fig. 3]; i.e., these singularities are on the positive and negative real axes

in the complex- \mathbf{q} plane, respectively. They lie farthest from the origin because the radius of convergence $R(z)$ assumes its maximum value at these points [panel (a) of Fig. 3]; $R(z)$ assumes its minimum value R_m at $z = \{\frac{\pi}{4}, \frac{3\pi}{4}\}$; here, $\theta(z) = \frac{\pi}{2}$. Thus, singularities for $z = \{\frac{\pi}{4}, \frac{3\pi}{4}\}$ are closest to the origin and are positioned on the imaginary axis $\Re(\mathbf{q}) = 0$. In particular, when $t^2 > R_m$, where $R_m = R(z = \{\frac{\pi}{4}, \frac{3\pi}{4}\})$, the fields in Fig. 2 develop early-time resonances. The minimum radius of convergence $R_m \simeq 1.17$ or $t_m \simeq 1.08$ for all fields (see Figs. 3 and 4); however, early-time resonances appear more prominently in ω_{N_t} than in u_{N_t} and v_{N_t} (see Fig. 2).

In Fig. 4, we plot $(R(z), \theta(z))$, for different values of z in the complex \mathbf{q} plane, by using polar coordinates. These singularities form of an approximately elliptical eye, which is centered at the origin and compressed along the $\Im(\mathbf{q})$ axis. The arrangement of such complex singularities in the form of an eye was first reported for time-Taylor expansions of the 1D inviscid Burgers equation²⁸ where the eye occurs in the complex- t plane. Given the symmetries of initial conditions that we use, these eyes occur in the complex- \mathbf{q} plane (see Fig. 4). In panel (c) of Fig. 3, we plot the exponent $\nu(z)$ of the convergence-limiting singularities for all the fields; here, we observe that ν takes non-integer values that depend on z . This z dependence is significant only near $z = \{0, \frac{\pi}{2}, \pi\}$; otherwise, $\nu \simeq \frac{1}{2}$ for u , and $\nu = -\frac{1}{2}$ for ω and v . We cannot obtain accurate estimates for singularities that lie arbitrary close to the real axis in Fig. 4. This is because the MR method is effective only when the series has settled down to its final regular behavior. Given finite-resolution and finite-precision errors, the truncated Taylor series that we use in Eq. (14) does not contain enough terms to capture this behavior. (See Appendix B for details.)

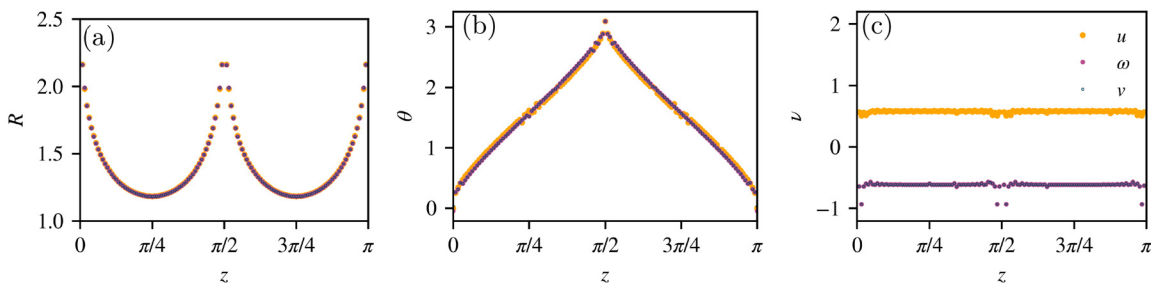


FIG. 3. Plots vs z of the estimates of (a) R , (b) θ , and (c) ν , obtained from u_n (orange), ω_n (pink), and v_n (blue), for $z \in \mathbf{X}_{256}$ and $n \leq N_t = 100$, by using the MR method. A full nonlinear fit of B_k^2 in Eq. (16a) is performed by using the LMFIT package in Python.

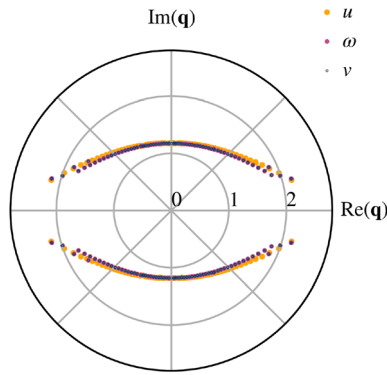


FIG. 4. Polar plot, in the complex- q plane, of $R(z)$ vs $\theta(z)$, depicting the positions of convergence-limiting complex singularities $\mathbf{q}_* = Re^{i\theta}$, as well as their complex-conjugates, for u (yellow), ω (pink), and v (blue) at $z \in \mathbf{X}_{N=256}$. The singularities are arranged in the shape of an eye, which is squashed along the $\Im(\mathbf{q})$ axis and is centered at the origin.

B. 3D-axisymmetric wall-bounded incompressible Euler equation

We use the singular initial condition proposed by Ref. 1 for this model to obtain

$$u_0^1(r, z) = e^{-30(1-r^2)^4} \sin\left(\frac{2\pi}{L}z\right), \tag{17a}$$

$$\omega_0^1(r, z) = 0, \quad \text{and} \quad \psi_0^1(r, z) = 0, \tag{17b}$$

where $L = 2\pi$ (Note that Refs. 1 and 2 use $L = 1/6$). For every point $(r, z) \in \mathbf{X}_{N,M}$, we use our Fourier–Chebyshev pseudospectral method² to compute $u_n^1(\mathbf{X}_{N,M})$ and $\omega_n^1(\mathbf{X}_{N,M})$ via the recursion relations (11a) and (11b), respectively. We then solve the Poisson problem (11c) and (11d) for $\psi_n^1(\mathbf{X}_{N,M})$ by using the Tau Poisson solver in Fourier–Chebyshev spectral space.² The time-Taylor coefficients for the radial and axial velocities, $u_n^r(\mathbf{X}_{N,M})$ and $u_n^z(\mathbf{X}_{N,M})$, are then computed from $\psi_n^1(\mathbf{X}_{N,M})$ (see Sec. II B 2).

In Fig. 5, we present the sign-coded heat map of the absolute values of the coefficients u_n^1 , ω_n^1 , and ψ_n^1 for $n \leq 86$ evaluated at the collocation points $(r_N, z) \in \mathbf{X}_{N,M}$ where $(N = 128, M = 256)$; r_N is the Chebyshev node that lies closest to the boundary at $r = 1$. As in Fig. 1, the coefficients with positive (negative) signs are shown in red (blue),

with log scale (base 10) color bars; the coefficients vanish identically (e.g., for odd orders in u_n^1) or fall below 10^{-40} in white regions. The odd-order coefficients for u_n^1 and the even-order coefficients for ω_n^1 and u_n^z vanish identically because of the symmetry of the initial condition (17).

In Fig. 6, we plot, as a function of (r, z) , the time-Taylor series truncated at $N_t = 86$ and evaluated at time $t = 2.6$ for the fields (a) $u_{N_t}^1(\mathbf{X}_{N,M})$, (b) $\omega_{N_t}^1(\mathbf{X}_{N,M})$, and (c) $u_{N_t}^z(\mathbf{X}_{N,M})$. Early-time resonances emerge at the wall ($r = 1$) in all fields. In Fig. 7, we plot these fields vs z , at $r = r_N$. These plots show clearly the development of oscillations at $z = \{\frac{\pi}{4}, \frac{3\pi}{4}\}$ (in Fig. 6, also at $\{\frac{5\pi}{4}, \frac{7\pi}{4}\}$). In Fig. 4 of Ref. 2, we have reported the emergence of tygers, $z = \{\frac{\pi}{2}, \frac{3\pi}{2}\}$ in all fields in this model, while using traditional Fourier–Chebyshev pseudospectral methods, for these initial data. We again emphasize that (as in the 1D HL model) these tygers are different from the early-time resonances in Fig. 7.

Given that the even-order coefficients for $u_n^1(r_N, z)$ and the odd-order coefficients for $\omega_n^1(r_N, z)$, $u_n^z(r_N, z)$ are identically zero (Fig. 5), the time-Taylor series can be rewritten for the variable $q = t^2$ [cf. Eq. (14) for the 1D HL model],

$$u_{N_t}^1(r_N, z, q) = \sum_{n=0}^{N_t/2} u_{2n}^1(r_N, z) q^n; \tag{18a}$$

$$\omega_{N_t}^1(r_N, z, q) = q^{1/2} \sum_{n=0}^{N_t/2} \omega_{2n+1}^1(r_N, z) q^n; \tag{18b}$$

$$u_{N_t}^z(r_N, z, q) = q^{1/2} \sum_{n=0}^{N_t/2} u_{2n+1}^z(r_N, z) q^n.$$

For a given field, we also note that the non-zero time-Taylor coefficients, computed at a point z near the wall r_N by using the initial data (17), have a pattern of alternating signs (cf. Sec. III A for the 1D HL model). Thus, we can use the MR methods as we did for the 1D HL model in Eq. (15). For each value of $z \in \mathbf{X}_{N,M}$ near the wall at r_N , we construct $B_k^2(z)$ as in Eq. (16a). Our estimates for R , θ , and ν , which we obtain by using the LMFIT package³⁹ in Python as for the 1D HL model, are shown in panels (a)–(c) of Fig. 8, where we superpose the estimates for $u_{N_t}^1(r_N, z_j)$ (yellow), $\omega_{N_t}^1(r_N, z_j)$ (pink), and $u_{N_t}^z(r_N, z_j)$ (blue).

The convergence-limiting singularities for the series, evaluated at the wall for $z = \{0, \pi\}$, are located on the positive real axis because

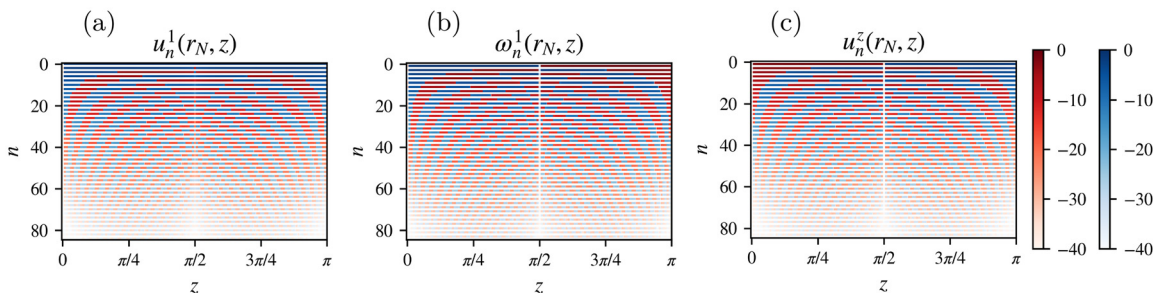


FIG. 5. Sign-coded heat maps of the absolute values of the time-Taylor coefficients (a) $u_n^1(r_N, z)$, (b) $\omega_n^1(r_N, z)$, and (c) $u_n^z(r_N, z)$, for $n \leq N_t = 86$ and evaluated at $r_N, z \in \mathbf{X}_{N,M}$, where $(N = 128, M = 256)$. The coefficients with positive (negative) signs are shown in red (blue); $u_n^1(r_N, z)$ vanish identically for odd n (white bands); and $\omega_n^1(r_N, z)$ and $u_n^z(r_N, z)$ vanish identically for even n , because of the symmetry of the initial data. We use a log scale (base 10) for the color bar.

23 October 2024 07:51:49

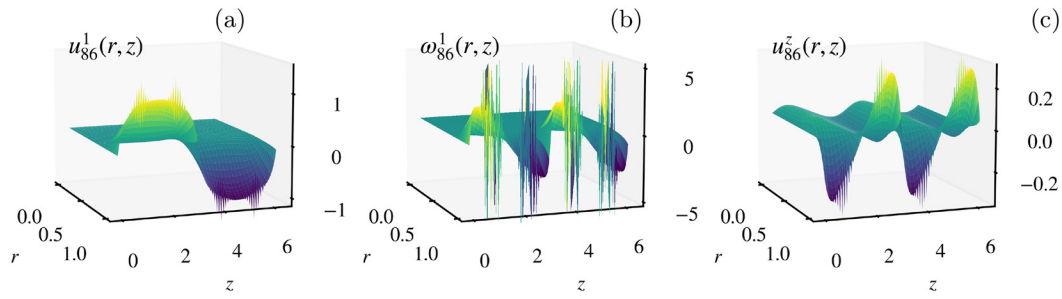


FIG. 6. Surface plots vs (r, z) of the time-Taylor-series approximations of the fields (a) u^1 , (b) ω^1 , and (c) u^z , truncated at $N_t = 86$ and evaluated at time $t = 2.6$ on a Fourier–Chebyshev collocation grid $X_{N,M}$, where $(N = 128, M = 256)$. We see the development of early-time resonances in all fields near the wall at $r = 1$. These resonant oscillations are localized around $z = \{\frac{\pi}{4}, \frac{3\pi}{4}, \frac{5\pi}{4}, \frac{7\pi}{4}\}$; they grow in amplitude and spread outwards in time.

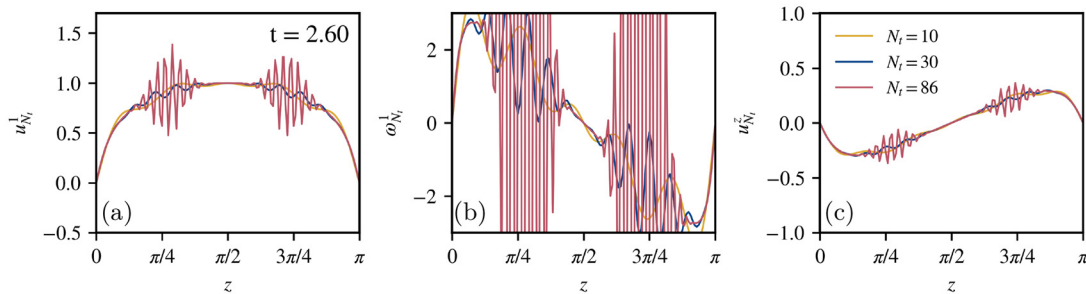


FIG. 7. Plots vs z of the truncated time-Taylor-series approximations for the fields (a) $u^1_{N_t}(r_N, z, t)$, (b) $\omega^1_{N_t}(r_N, z, t)$, and (c) $u^z_{N_t}(r_N, z, t)$, evaluated at time $t = 2.6$ and summed for three orders of truncation, namely, $N_t = 10$ (yellow), 30 (blue), and 100 (red). Early-time resonances occur in all three fields as oscillatory structures localized around $z = \{\frac{\pi}{4}, \frac{3\pi}{4}\}$. The oscillations have the largest amplitude for $\omega^1_{N_t}$.

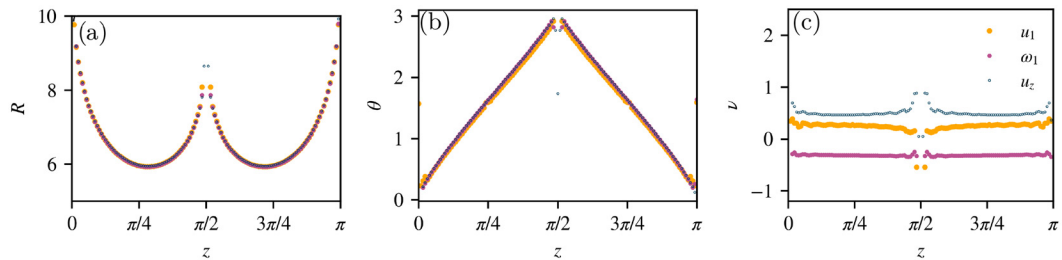


FIG. 8. Plots vs z of the estimates of (a) R , (b) θ , and (c) ν , obtained from $u^1_n(r_N, z)$ (orange), $\omega^1_n(r_N, z)$ (pink), and $u^z_n(r_N, z)$ (blue), for $z \in X_{N,M}$, where $(N = 128, M = 256)$ and $n \leq N_t = 86$, using the MR method. A full nonlinear fit of $B^2_{\tilde{q}}$ in Eq. (16a) is performed by using the LMFIT package in Python. For more details on the MR method, see Appendix B.

$\theta(z) = 0$ (cf. Fig. 4 for the 1D HL model); these singularities are situated farthest from the origin in the complex- \mathbf{q} plane. The estimates for $R(z)$ in Fig. 8(a) are not arranged symmetrically about $z = \{\frac{\pi}{4}, \frac{3\pi}{4}\}$ [unlike in Fig. 3(a) for the 1D HL model]. Here, the convergence-limiting singularities with the smallest radius of convergence ($R_m \simeq 5.95$) occur at $z \simeq 0.88 > \frac{\pi}{4}$ and $z \simeq 2.26 < \frac{3\pi}{4}$ in Fig. 8(a). In the complex- \mathbf{q} plane, the arrangement of the convergence-limiting singularities is in the form of an eye (Fig. 9), whose center lies on the real axis but is displaced to the right of the origin, for all three fields: u^1 (orange), ω^1 (pink), and u^z (blue), because of the asymmetry of $R(z)$ mentioned above. In panel (c) of Fig. 8, we plot the order ν of the convergence-limiting singularities obtained for the fields u^1 (yellow),

ω^1 (pink), and u^z (blue). For u^1 , ν takes non-integer values which depend on z ; for z near $\frac{\pi}{2}$, it is negative but otherwise remains positive. For ω^1 , $\nu \simeq -1/3$; and for u^z , $\nu \in (0.5, 1)$. (See Appendix B for estimates for R obtained at different distances r .)

IV. CONCLUSIONS

We have shown how to adapt the methods introduced in Ref. 28 to investigate early-time resonances in two PDEs that have attracted considerable attention recently^{1,2,30,37,38,40} in the context of possible finite-time singularities in ideal hydrodynamical systems. The first is the 1D HL model and the second is the 3DAE; the former is related approximately to the latter (see, e.g., Refs. 1, 2, and 30). We have used

23 October 2024 07:51:49

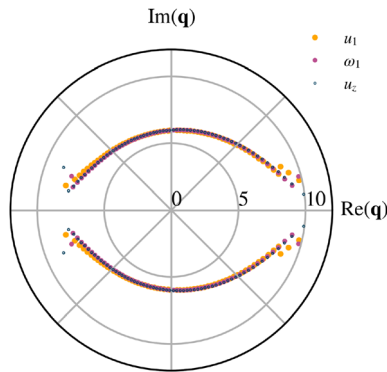


FIG. 9. Polar plot in complex- \mathbf{q} plane of $R(z)$ vs $\theta(z)$ depicting the position of convergence-limiting complex singularities $\mathbf{q}_s = Re^{i\theta}$ as well as their complex-conjugates, for u^1 (yellow), ω^1 (pink), and u^2 (blue) at $r = r_N$ and $z \in \mathbf{X}_{N,M}$, where ($N = 128$, $M = 256$). The singularities are arranged in the shape of an eye, which is squashed along the $\Re(\mathbf{q})$ axis; the center of the eye is displaced to the right of the origin.

initial data from earlier studies of singularities for both these PDEs and employed our pseudospectral Fourier–Chebyshev method,² with quadruple-precision arithmetic, to compute the time-Taylor-series coefficients of the flow fields, up to a high order [$N_t = 100$ (1DHL) and $N_t = 86$ (3DAE)]. The resulting approximations display early-time resonances, which we have studied in detail. In particular, we have demonstrated that the initial spatial location of these resonances is different from that for the tygers, which we have obtained in Ref. 2. We have analyzed the time-Taylor-series coefficients, by using the MR method, to extract $R(z)$, $\theta(z)$, and $\nu(z)$, and thence the location and nature of the convergence-limiting singularities. We have found that these singularities are distributed around the origin, in the complex- t^2 plane, along two curves that resemble an approximately elliptical eye.

The connection between complex-space and complex-time singularity landscapes is a challenging problem that is now being explored for ideal hydrodynamical PDEs such as the inviscid, unforced 1D Burgers equation.²⁸ Our work has enlarged the scope of such studies by investigating such connections for the 1DHL and 3DAE systems. It is important to understand the link (if any) between tygers, in Galerkin-truncated pseudospectral studies, and the early-time resonances, in truncated time-Taylor expansions of solutions of PDEs.

Pseudospectral approximations are Galerkin-truncated at the dealiasing cutoff K_G ; this gives a threshold length-scale $\lambda_G = \frac{2\pi}{K_G}$. When the flow develops length-scales smaller than λ_G , they cannot be resolved accurately; then, tygers emerge in the flow following the entry of the nearest complex-space singularity into the analyticity-strip of threshold width λ_G .^{2,23,26} Recently, modified pseudospectral schemes have been proposed for the mitigation of tygers and for extending the time until which we have an accurate representation of the flow.^{41–43} These methods apply a controlled dissipation to prevent thermalization in the Galerkin-truncated pseudospectral approximations, which would otherwise be energy-conserving.⁴⁴ Boot-strapping methods gradually increase the resolution of the DNS at times when spectral convergence is almost exhausted; this is tantamount to decreasing λ_G such that the limiting complex-space singularity never crosses into the threshold strip.⁴⁵

When we use time-Taylor-series methods, we truncate the series beyond order N_t for tractability. The radius of convergence R of the resulting Taylor series is limited by the nearest complex-time singularity, and for times $t > R$, early-time resonances develop in the series approximations. We can circumvent this limitation and probe the real finite-time singularity by performing analytic-continuation along the real-axis à la Weierstrass; however, this technique is arduous even for the 1D inviscid Burgers equation. Recent work by Ref. 28 has studied tyger-purging methods and UV-iteration methods to build time-Taylor-series representations of the solution, to the 1D inviscid Burgers equation, which are free from early-time resonances. These UV-iteration methods lie beyond the scope of this paper; we will develop them, for the models we consider, in future studies.

It is thereby clear that, when we use truncated pseudospectral or time-series methods to approximate discontinuous (shock or cusp-like) solutions, we are limited by truncation artifacts: tygers and early-time resonances, respectively. Despite this limitation, the analyticity-strip method (used in conjunction with pseudospectral schemes) and the time-series methods that we use here provide powerful means of studying the complex-space and complex-time landscapes for the potentially singular solutions.

ACKNOWLEDGMENTS

We thank SERB, CSIR, and NSM (India) for their support and SERC (IISc) for computational resources. We thank J. K. Alageshan, U. Frisch, K. V. Kiran, T. Matsumoto, C. Rampf, and S. S. Ray for useful discussions.

AUTHOR DECLARATIONS

Conflict of Interest

The authors have no conflicts to disclose.

Author Contributions

Sai Swetha Venkata Kolluru: Conceptualization (lead); Data curation (equal); Formal analysis (equal); Investigation (equal); Methodology (equal); Project administration (equal); Validation (equal); Visualization (equal); Writing – original draft (equal); Writing – review & editing (equal). **Rahul Pandit:** Conceptualization (supporting); Funding acquisition (lead); Project administration (equal); Resources (lead); Supervision (equal); Writing – review & editing (equal).

DATA AVAILABILITY

The data that support the findings of this study are available from the corresponding author upon reasonable request.

APPENDIX A: CODE

The following MATHEMATICA 12 code computes analytical closed-form expressions for the time-Taylor coefficients; $u_n(z)$ is stored in `u[n, z]`, $\omega_n(z)$ in `w[n, z]`, and $v_n(z)$ in `v[n, z]`. Here, `Ntmax` represents the order of truncation N_t . The initial conditions are given in lines 4–6. Recursion relations given in Eq. (3) are given in lines 8–10. The coefficients are then appended to `listc` which can ultimately be stored symbolically and later retrieved.

LISTING 1. Mathematica 12 code.

```

1 listc = {}; Ntmax = 70; f[n_] = Floor[(n - 1)/2];
2 HilbertTransform[f_, x_, X_] := Module[{fp = FourierParameters -> {1, -1}, k},
   InverseFourierTransform[-I(2 HeavisideTheta[k] - 1) * FourierTransform[f, x, k, fp], k, X, fp]];
3
4 u[0, z_] := (Sin[z])^2;
5 w[0, z_] := 0;
6 v[0, z_] := Integrate[HilbertTransform[w[0, x], x, z], z];
7
8 w[n_, z_] := w[n, z] = If[EvenQ[n], 0, (-Sum[If[i! = (n - 1 - i), v[i, z] D[w[n - 1 - i, z], z] + v[
   [n - 1 - i, z] D[w[i, z], z], v[i, z] D[w[i, z], z]], {i, 0, f[n], 1}] + D[u[n - 1, z], z])/n];
9 u[n_, z_] := u[n, z] = If[OddQ[n], 0,
10   (-Sum[If[i! = (n - 1 - i), v[i, z] D[u[n - 1 - i, z], z] + v[n - 1 - i, z] D[u[i, z], z], v[i, z]
   D[u[i, z], z]], {i, 0, f[n], 1}))/n];
11 v[n_, z_] := v[n, z] = If[EvenQ[n], 0, Integrate[HilbertTransform[w[n, x], x, z], z]];
12
13 Do[nn = n; AppendTo[listc, {n, u[n, z], w[n, z], v[n, z]}], {n, 0, Ntmax}];

```

APPENDIX B: MERCER-ROBERTS METHOD

For perturbation series where the coefficients' signs follow a non-trivial pattern, Mercer and Roberts²⁹ generalized the Domb-Sykes method to allow for a pair of complex-conjugate singularities.

Consider a model function that has complex-conjugate singularities at t_* and \bar{t}_* ,

$$u(t) = \left(1 - \frac{t}{t_*}\right)^\nu + \left(1 - \frac{t}{\bar{t}_*}\right)^\nu; \quad \text{where } t_* := Re^{i\theta}. \quad (B1)$$

For $|t| < R$, the model function u has the following Taylor expansion around $t = 0$:

$$u(t) = \sum_{n=0}^{\infty} 2(-1)^n \binom{\nu}{n} R^{-n} \cos(n\theta) t^n. \quad (B2)$$

Mercer and Roberts showed that R, θ , and ν can be determined by relating the model function in Eq. (B2) to the original series $u(t) = \sum_{n=0}^{\infty} u_n t^n$. For each 4-tuple of u_n , we construct

$$B_k^2 = \frac{u_{k+1}u_{k-1} - u_k^2}{u_k u_{k-2} - u_{k-1}^2}, \quad (B3a)$$

$$\cos \theta_k = \frac{1}{2} \left(\frac{u_{k-1}B_k}{u_k} + \frac{u_{k+1}}{u_k B_k} \right), \quad (B3b)$$

where $k = 2, 3, \dots$. The leading-order behavior is then obtained by substituting Eq. (B2) into Eq. (B3),

$$B_k = \frac{1}{R} - \left(\frac{\nu + 1}{R}\right) \frac{1}{k} + \left(\frac{\nu + 1}{2R} \frac{\sin(2k - 1)\theta}{\sin \theta}\right) \frac{1}{k^2} + \mathcal{O}\left(\frac{1}{k^3}\right), \quad (B4a)$$

$$\cos \theta_k = \cos \theta + \left[\cos \theta (\nu + 1) \left(1 - \frac{\cos(2k - 1)\theta}{\cos \theta}\right) \right] \frac{1}{k^2} + \mathcal{O}\left(\frac{1}{k^3}\right). \quad (B4b)$$

For large k , we can extract $1/R$ from the intercept on the vertical axis, in the plot of B_k vs $1/k$, and $\cos \theta$ from the plot of $\cos \theta_k$ vs $1/k^2$.

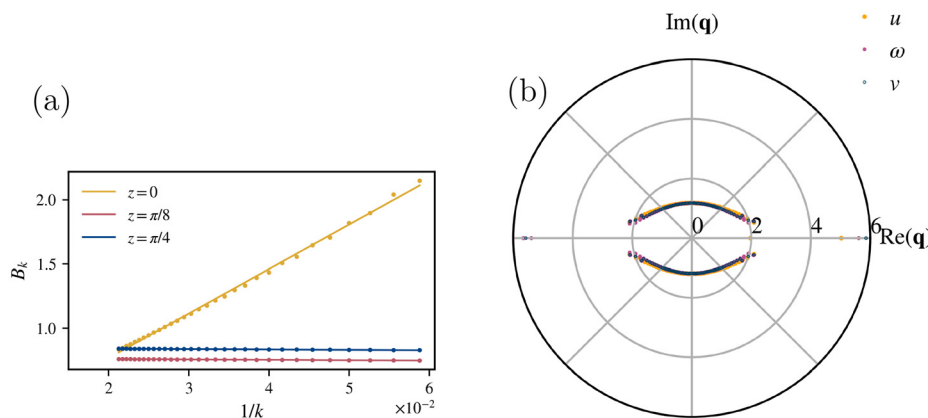


FIG. 10. For the 1D HL model: (a) Plots vs $1/k$ of $B_k(z)$ computed from $u_n(z)$ using Eq. (16a), for $z = 0$ (yellow), $\pi/8$ (red), and $\pi/4$ (blue). (b) Extended polar plot in complex- q plane of $R(z)$ vs $\theta(z)$ depicting the position of convergence-limiting complex singularities $q_* = Re^{i\theta}$ as well as their complex-conjugates, for u (yellow), ω (pink), and v (blue). Here, we note the singularities on the real-axis obtained using MR method for this model. The time-Taylor coefficients are estimated on a uniform grid of $X_{N=256}$ using quadruple-precision Fourier-pseudospectral methods.

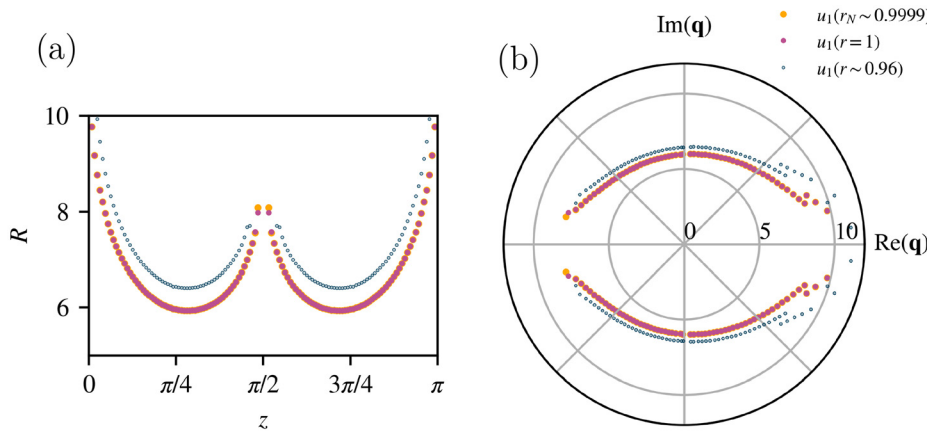


FIG. 11. For 3DAE: (a) Plots vs z of the estimates of R and (b) polar plot, in the complex- q plane, of $R(z)$ vs $\theta(z)$ depicting the position of convergence-limiting complex singularities $\mathbf{q}_* = Re^{i\theta}$ as well as their complex-conjugates, obtained from $u_n^1(r_N, z)$ for $z \in \mathbf{X}_{N,M}$, where $(N = 128, M = 256)$ and $n \leq N_t = 86$, using the MR method; the estimates are shown for different distances from the wall at $r \in \{0.96, r_N, 1\}$ (see legend). Here, we see that the eye is shifted for all r , and the MR estimates worsen far from the wall (where the singularity precipitates).

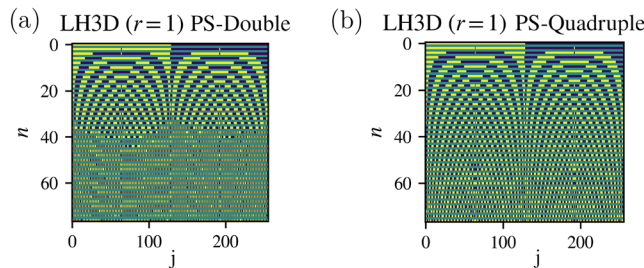


FIG. 12. Sign-coded heat maps of the time-Taylor coefficients $u_n^1(r=1, z_j)$ obtained from Fourier–Chebyshev pseudospectral scheme for $(N = 128, M = 256)$ (a) using double-precision arithmetic and (b) quadruple-precision arithmetic, respectively. The coefficients with positive (negative) signs are shown in yellow (blue); $u_n^1(r=1, z_j)$ vanish identically for odd n (green bands) because of the symmetry of the initial data.

In Fig. 10(a), we show the plots vs $1/k$ of B_k , obtained from $u_n(z)$ in Eq. (3a) for the 1D HL model, at the spatial locations $z = \{0, \frac{\pi}{8}, \frac{\pi}{4}\}$ in yellow, red, and blue, respectively. For these values of z , the leading-order linear behavior dominates asymptotically. For θ close to $\{0, \pm\pi\}$, the estimators in Eq. (B4) become unreliable as high-order terms are not negligible.

In Fig. 10(b), we show the eye, including the MR estimates obtained by using the linear forms [Fig. 10(a)], exactly at the singular z points. In Fig. 11(a), we show the estimates for R , obtained as above, at different distances r from the wall. In particular, we compute the time-Taylor approximations at the wall $r = 1$, at $r = r_N$ (as before), and at an interior point $r = 0.96$. All these values of r yield

eyes with shifted centers of $R(z)$ about $z = \{\frac{\pi}{4}, \frac{3\pi}{4}\}$ persists. In Fig. 11(b), we plot the associated eyes in the complex- q plane; the center of the eye is shifted from the origin for all the choices of r above. To the best of our knowledge, the eye associated with the 3DAE is the first with a shifted center; this shift remains to be understood.

APPENDIX C: COMPARISON OF DOUBLE AND QUADRUPLE-PRECISION ESTIMATES FOR THE 3DAE MODEL

In Fig. 12, we present the sign-coded heat map of the time-Taylor coefficients $u_n^1(r=1, z)$ for $n \leq 86$ estimated using the recursion relation in Eq. (11a) by Fourier–Chebyshev pseudospectral methods described in Sec. II B 3. In panel (a), we present the estimates obtained using double-precision arithmetic: here, we see that the sign pattern is lost around $n \simeq 40$, and the lower half of the heat map appears noisy. Beyond this order, the MR coefficients B_k^2 computed from $u_n^1(r=1, z)$ shown in Fig. 13(a) have a haphazard dependence on k , and the MR form (B4) is no longer seen. When we employ quadruple-precision arithmetic, we find that the sign-pattern is restored for $n \geq 40$ [see panel (b) of Fig. 12] and is akin to that seen in the 1D HL model (cf. Fig. 1). In Fig. 13(b), we plot the MR coefficient B_k^2 obtained from $u_n^1(r=1, z)$ vs k ; here, we observe that the round-off errors are unimportant until $n \geq 86$. In this range, B_k^2 has a systematic dependence on k from which we obtain accurate estimates for R , θ , and ν as discussed in Sec. III B.

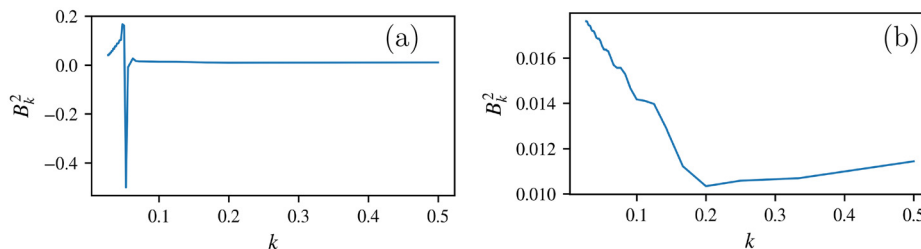


FIG. 13. Plots vs k of the MR-coefficient B_k^2 computed using Eq. (B3) from the time-Taylor coefficients $u_n^1(r=1, z)$; the coefficients are obtained from Fourier–Chebyshev pseudospectral schemes for $(N = 128, M = 256)$: (a) using double-precision arithmetic and (b) quadruple-precision arithmetic, respectively.

REFERENCES

- ¹G. Luo and T. Y. Hou, "Potentially singular solutions of the 3D axisymmetric Euler equations," *Proc. Natl. Acad. Sci. U. S. A.* **111**(36), 12968–12973 (2014).
- ²S. S. V. Kolluru, P. Sharma, and R. Pandit, "Insights from a pseudospectral study of a potentially singular solution of the three-dimensional axisymmetric incompressible Euler equation," *Phys. Rev. E* **105**(6), 065107 (2022).
- ³P. Constantin and C. Foias, *Navier-Stokes Equations* (University of Chicago Press, 1988).
- ⁴C. R. Doering and J. D. Gibbon, *Applied Analysis of the Navier-Stokes Equations* (Cambridge University Press, 1995).
- ⁵P. Constantin, "Euler equations, Navier-Stokes equations and turbulence," in *Mathematical Foundation of Turbulent Viscous Flows: Lectures Given at the CIME Summer School Held in Martina Franca, Italy, September 1–5, 2003* (Springer, 2005), pp. 1–43.
- ⁶J. Gibbon, "The three-dimensional Euler equations: How much do we know?," *Physica D* **237**(14–17), 1894–1904 (2008).
- ⁷L. Onsager, "Statistical hydrodynamics," *Nuovo Cim.* **6**(Suppl), 279–287 (1949).
- ⁸P. Constantin, E. Weinan, and E. S. Titi, "Onsager's conjecture on the energy conservation for solutions of Euler's equation," *Commun. Math. Phys.* **165**(1), 207–209 (1994).
- ⁹G. L. Eyink and K. R. Sreenivasan, "Onsager and the theory of hydrodynamic turbulence," *Rev. Mod. Phys.* **78**(1), 87 (2006).
- ¹⁰G. L. Eyink, "Dissipative anomalies in singular Euler flows," *Physica D* **237**(14), 1956–1968 (2008).
- ¹¹C. De Lellis and L. Székelyhidi, Jr., "Dissipative Euler flows and Onsager's conjecture," *J. Eur. Math. Soc.* **16**(7), 1467–1505 (2014).
- ¹²R. H. Morf, S. A. Orszag, and U. Frisch, "Spontaneous singularity in three-dimensional inviscid, incompressible flow," *Phys. Rev. Lett.* **44**(9), 572 (1980).
- ¹³D. Gaunt and A. Guttman, "Asymptotic analysis of coefficients," in *Phase Transitions and Critical Phenomena* (Academic Press, 1974), Vol. 3, pp. 181–243.
- ¹⁴C. Domb and M. F. Sykes, "On the susceptibility of a ferromagnetic above the curie point," *Proc. R. Soc. London, Ser. A* **240**(1221), 214–228 (1957).
- ¹⁵C. M. Bender and S. A. Orszag, *Advanced Mathematical Methods for Scientists and Engineers I: Asymptotic Methods and Perturbation Theory* (Springer Science & Business Media, 2013).
- ¹⁶M. E. Brachet, D. I. Meiron, S. A. Orszag, B. Nickel, R. H. Morf, and U. Frisch, "Small-scale structure of the Taylor–Green vortex," *J. Fluid Mech.* **130**, 411–452 (1983).
- ¹⁷M. E. Brachet, D. Meiron, S. Orszag, B. Nickel, R. Morf, and U. Frisch, "The Taylor–Green vortex and fully developed turbulence," *J. Stat. Phys.* **34**(5), 1049–1063 (1984).
- ¹⁸R. Pelz and Y. Gulak, "Evidence for a real-time singularity in hydrodynamics from time series analysis," *Phys. Rev. Lett.* **79**(25), 4998 (1997).
- ¹⁹R. Morf, S. Orszag, D. Meiron, M. Meneguzzi, and U. Frisch, "Analytic structure of high Reynolds number flows," in *Seventh International Conference on Numerical Methods in Fluid Dynamics* (Springer, 1981), pp. 292–298.
- ²⁰U. Frisch and R. Morf, "Intermittency in nonlinear dynamics and singularities at complex times," *Phys. Rev. A* **23**(5), 2673 (1981).
- ²¹D. I. Meiron, G. R. Baker, and S. A. Orszag, "Analytic structure of vortex sheet dynamics. Part 1. Kelvin–Helmholtz instability," *J. Fluid Mech.* **114**, 283–298 (1982).
- ²²K. Ohkitani and J. D. Gibbon, "Numerical study of singularity formation in a class of Euler and Navier–Stokes flows," *Phys. Fluids* **12**(12), 3181–3194 (2000).
- ²³C. Sulem, P.-L. Sulem, and H. Frisch, "Tracing complex singularities with spectral methods," *J. Comput. Phys.* **50**(1), 138–161 (1983).
- ²⁴R. M. Kerr, "Evidence for a singularity of the three-dimensional, incompressible Euler equations," *Phys. Fluids A* **5**(7), 1725–1746 (1993).
- ²⁵C. Cichowlas and M. Brachet, "Evolution of complex singularities in Kida–Pelz and Taylor–Green inviscid flows," *Fluid Dyn. Res.* **36**(4–6), 239 (2005).
- ²⁶S. S. Ray, U. Frisch, S. Nazarenko, and T. Matsumoto, "Resonance phenomenon for the Galerkin-truncated Burgers and Euler equations," *Phys. Rev. E* **84**, 016301 (2011).
- ²⁷S. D. Murugan and S. S. Ray, "Genesis of thermalization in the three-dimensional, incompressible, Galerkin-truncated Euler equation," *Phys. Rev. Fluids* **8**(8), 084605 (2023).
- ²⁸C. Rampf, U. Frisch, and O. Hahn, "Eye of the tyger: Early-time resonances and singularities in the inviscid Burgers equation," *Phys. Rev. Fluids* **7**(10), 104610 (2022).
- ²⁹G. Mercer and A. Roberts, "A centre manifold description of contaminant dispersion in channels with varying flow properties," *SIAM J. Appl. Math.* **50**(6), 1547–1565 (1990).
- ³⁰K. Choi, T. Y. Hou, A. Kiselev, G. Luo, V. Sverak, and Y. Yao, "On the finite-time blowup of a one-dimensional model for the three-dimensional axisymmetric Euler equations," *Commun. Pure Appl. Math.* **70**(11), 2218–2243 (2017).
- ³¹M. Frigo and S. G. Johnson, "The design and implementation of FFTW3," *Proc. IEEE* **93**(2), 216–231 (2005).
- ³²A. J. Majda and A. L. Bertozzi, *Vorticity and Incompressible Flow* (Cambridge University Press, 2002), Vol. 27.
- ³³T. Y. Hou and C. Li, "Dynamic stability of the three-dimensional axisymmetric Navier–Stokes equations with swirl," *Commun. Pure Appl. Math.* **61**(5), 661–697 (2008).
- ³⁴J.-G. Liu and W.-C. Wang, "Characterization and regularity for axisymmetric solenoidal vector fields with application to Navier–Stokes equation," *SIAM J. Math. Anal.* **41**(5), 1825–1850 (2009).
- ³⁵R. Peyret, *Spectral Methods for Incompressible Viscous Flow* (Springer Science & Business Media, 2013), Vol. 148.
- ³⁶M. Van Dyke, "Analysis and improvement of perturbation series," *Q. J. Mech. Appl. Math.* **27**(4), 423–450 (1974).
- ³⁷D. Barkley, "A fluid mechanic's analysis of the teacup singularity," *Proc. R. Soc. London, Ser. A* **476**, 20200348 (2020).
- ³⁸T. Hertel, N. Besse, and U. Frisch, "The Cauchy–Lagrange method for 3D-axisymmetric wall-bounded and potentially singular incompressible Euler flows," *J. Comput. Phys.* **449**, 110758 (2021).
- ³⁹M. Newville, T. Stensitzki, D. B. Allen, M. Rawlik, A. Ingargiola, and A. Nelson, "Lmfit: Non-linear least-square minimization and curve-fitting for python," *Astrophysics Source Code Library* (2016), pp. ascl-1606.
- ⁴⁰G. Luo and T. Y. Hou, "Toward the finite-time blowup of the 3D axisymmetric Euler equations: A numerical investigation," *Multiscale Model. Simul.* **12**(4), 1722–1776 (2014).
- ⁴¹S. D. Murugan, U. Frisch, S. Nazarenko, N. Besse, and S. S. Ray, "Suppressing thermalization and constructing weak solutions in truncated inviscid equations of hydrodynamics: Lessons from the Burgers equation," *Phys. Rev. Res.* **2**(3), 033202 (2020).
- ⁴²V. S. S. Kolluru, N. Besse, and R. Pandit, "Novel spectral methods for shock capturing and the removal of tygers in computational fluid dynamics," *arXiv:2402.17688* (2024).
- ⁴³N. Besse, "Analysis of the spectral relaxation method and the spectral purging method for nonlinear conservation laws" (submitted).
- ⁴⁴P. C. Di Leoni, P. D. Mininni, and M. E. Brachet, "Dynamics of partially thermalized solutions of the Burgers equation," *Phys. Rev. Fluids* **3**(1), 014603 (2018).
- ⁴⁵M. E. Brachet, M. Bustamante, G. Krstulovic, P. D. Mininni, A. Pouquet, and D. Rosenberg, "Ideal evolution of magnetohydrodynamic turbulence when imposing Taylor–Green symmetries," *Phys. Rev. E* **87**(1), 013110 (2013).